Journal of Materials Chemistry A

ROYAL SOCIETY OF CHEMISTRY

PAPER

View Article Online
View Journal | View Issue

Cite this: J. Mater. Chem. A, 2025, 13, 22672

Structural transition in crystalline SiO_2 during mechanical amorphization under frictional shear†

Jin Jung Kweon, [a] Hoon Khim,[a] Yong-Hyun Kim [a] and Sung Keun Lee *[ab]

Mechanical milling increases structural disorder in crystalline materials, often resulting in a milling-induced amorphous phase. Prototypical SiO_2 crystals under mechanical shear during milling produce an amorphous phase that has potential for a wide range of applications, from battery anodes to catalyst substrates. Despite its importance, the extent of mechanical amorphization, the mechanochemical reactions, and atomic structure of amorphous materials formed *via* mechanical deformation remain elusive, because of the lack of experimental probes. Here, multinuclear solid-state nuclear magnetic resonance (NMR) allowed us to uncover the nature of the amorphization of crystalline SiO_2 produced by mechanical milling. The extensive NMR results reveal the milling-induced network depolymerization, hydroxylation, and topological contraction in SiO_2 networks during amorphization. In particular, extreme friction activates chemical interactions among the materials, forming *extrinsic* chemical bonds *via* mechanical chemical reactions during deformation under amorphization of SiO_2, indicating that the amorphous phase is not compositionally pure. The current findings with the extrinsic bonds may account for the anomalous increase in the storage capacity of amorphous materials formed by intense milling. The results establish the first quantitative kinetic model of a friction-induced increase in an amorphous SiO_2 complex by a dynamic milling process, identifying the threshold milling rate and duration for the formation of amorphous products. The current results provide predictive and practical guidelines for controlling amorphization through mechanical shear, shedding light on novel synthetic routes to diverse amorphous materials.

Received 1st May 2025
Accepted 30th May 2025

DOI: 10.1039/d5ta03462k

rsc.li/materials-a

1. Introduction

SiO_2 is a prototypical oxide with critical importance in condensed matter physics,[1] materials chemistry,[2–4] and geosciences,[5–7] and it has also been used as a potential Li-ion battery anode,[8] catalyst substrate,[9,10] and drug delivery system.[11,12] Its amorphous analog (a-SiO_2) can be produced by quenching molten SiO_2, or *via* chemical routes (*e.g.*, sol–gel synthesis or vapor deposition) and electron beam irradiation.[13] The high melting temperature of SiO_2 poses a challenge for the efficient production of a-SiO_2 by melt quenching, and conventional synthesis methods may not be feasible for the production of water-free a-SiO_2 nanoparticles with desirable physical properties.

The mechanical deformation of SiO_2 crystals (c-SiO_2) can be an effective a-SiO_2 synthesis technique,[14,15] overcoming the challenges associated with the synthesis of a-SiO_2 because amorphization *via* mechanical deformation can produce amorphous structures at room temperature (*i.e.*, high temperatures above the melting point for glass synthesis); the deformation of crystalline materials by milling can lead to the destruction of crystalline periodicity and formation of disordered atomic configurations. Mechanical energy can be applied by rapidly shaking or rotating the materials in the presence of hard balls in a closed bowl (*i.e.*, ball milling). The ball-milling process reduces the particle size by grinding the powders, thereby increasing the surface area.[16] Extensive mechanical milling can amorphize condensed matters (*i.e.*, mechanical amorphization), enabling the synthesis of amorphous materials that are difficult to prepare *via* conventional methods (*e.g.*, melt quenching). Hazardous or expensive solvents that are typically required for the chemical synthesis of amorphous materials (*e.g.*, sol–gel synthesis) may not be necessary for mechanical amorphization *via* milling, leading to the eco-friendly synthesis of novel amorphous materials. Additionally, mechanosynthesis has recently garnered attention as a viable method for material synthesis,[17] including techniques that involve mechanochemistry,[18,19] nanocomposites,[20–22] isotopic labelling,[23,24] multicomponent oxides,[25] mechanocatalysis,[26] and room-temperature thermochemical water splitting.[27] Specifically, ball-milled SiO_2 phases and composite systems have recently been used in Li-ion

[a]Laboratory of Physics and Chemistry of Earth and Planetary Materials, School of Earth & Environmental Sciences, Seoul National University, Seoul 08826, Korea. E-mail: sungklee@snu.ac.kr; Web: https://g2mat.snu.ac.kr

[b]Institute of Applied Physics, College of Natural Sciences, Seoul National University, Seoul 08826, Korea

† Electronic supplementary information (ESI) available. See DOI: https://doi.org/10.1039/d5ta03462k

battery anode materials,[28–30] where the amorphous phase of this SiO_2-based material demonstrated superior electrode material performance; however, the detailed atomistic origin remains unknown.

The mechanical energy from ball milling may also activate chemical reactions by forming defects. During ball milling, the milling media (*e.g.*, grinding balls and containers) or atmospheric components (*e.g.*, ambient moisture, oxygen, and nitrogen) can potentially interact with materials, affecting their structures and properties.[31,32] Thus, understanding the nature of such interactions is the key to designing mechanosynthetic routes. In particular, the structural characteristics of milling products and formation of milling-induced chemical bonds influence their macroscopic properties. Therefore, the desired functional properties can be optimized by controlling these structural parameters.[33,34] Furthermore, information on the deformation and amorphization of c-SiO_2 during mechanical milling can provide insight into earthquake rupture and slip weakening.[5,6,35]

Despite its importance and prospects in materials chemistry, condensed matter physics, and geosciences, the detailed nature of mechanical amorphization (*e.g.*, the degree of mechanical amorphization under varying deformation conditions and/or structures of amorphous materials synthesized *via* mechanical milling) remains unknown. This is because of the limitations of conventional experimental techniques such as X-ray scattering in the quantification of the fractions of amorphous phase and crystalline components, as well as in the probing of amorphous structures. Challenges arise from the complex chemical interactions of the materials with the surrounding moisture and/or milling media, which form extrinsic and intrinsic chemical bonds and contribute to the structural complexity of amorphous materials produced *via* mechanical milling. Quantitative information on the extent of mechanical amorphization and structural evolution, and proper identification of chemical bonds in ball-milled non-crystalline oxides, including a-SiO_2, remain to be explored.[29,32]

Solid-state nuclear magnetic resonance (NMR) is an ideal element-specific method for analyzing structural changes in mechanically deformed crystalline SiO_2 and its amorphization (see, *e.g.*, ref. 36–39). Solid-state ^{1}H magic-angle spinning (MAS) NMR is useful for the analysis of hydrogen speciation and quantification of hydrogen content (*e.g.*, ref. 40–42 and the references therein) and can thus effectively enable identification of the extent of potential hydration and hydroxylation during the mechanical milling of SiO_2. ^{29}Si MAS NMR spectroscopy can quantify the structural changes in the SiO_4 networks in a-SiO_2, which are often characterized by Q^n speciation (where n is the number of bridging oxygen atoms in the SiO_4 tetrahedra),[37] thereby revealing the evolution of amorphous network structures in SiO_2 during mechanical milling.[43] ^{1}H–^{29}Si heteronuclear correlation (HetCor) NMR enables the identification of potential water incorporation into SiO_2 under extreme friction.[37,44] Lastly, ^{17}O NMR spectroscopy directly probes the oxygen environment in amorphous oxides (*e.g.*, ref. 38 and 45–48 and the references therein). This technique can be used to explore the formation of novel oxygen environments during mechanical milling[49] and evaluate the chemical interactions between SiO_2 and the milling media.

Here, we note that '*amorphization*' during intense ball-milling refers to a transition *process* that occurs along with the loss of crystallinity in c-SiO_2. This process can be probed from the emergence of a broad diffraction peak and spectral broadening often observed unambiguously *via* high-resolution solid-state NMR. During amorphization under intense milling, the particle size could decrease, which may activate surface reactions. This could alter the chemical composition of the starting crystals. High-resolution spectroscopic techniques are necessary to understand the detailed nature of these interactions and for the identification of the species in the amorphous phases formed by milling of c-SiO_2 (hereafter, we refer to the 'a-SiO_2 product formed *via* intense ball-milling' as 'milled amorphous silica product'. The phase should consist of a chemical component (such as hydrogen) added during milling-induced frictional amorphization). In the current study, we employed multinuclear ^{1}H, ^{17}O, and ^{29}Si MAS NMR spectroscopy to quantitatively evaluate the structural changes in crystalline SiO_2 and the milled amorphous silica product *via* rapid frictional shear. Although the quantification of mechanical amorphization has been challenging, our study constitutes the first study to yield quantitative information on the degree of mechanical amorphization (*i.e.*, fractions of the milled amorphous silica product) at varying milling speeds and durations. Notably, we also discuss how experimental breakthroughs and conceptual advancements in mechanical amorphization in SiO_2 can lead to more effective optimization of the material synthesis routes for diverse non-crystalline oxides during milling, as well as other relevant processes during frictional slip.

2. Experimental

2.1. Sample preparation

Quartz (SiO_2) powder (≥99.995% trace metal basis, a few hundred μm in size on average) purchased from Sigma-Aldrich was deformed *via* milling at 200, 400, 600, and 800 rpm (revolutions per minute) under a milling duration of 5 h using a planetary ball mill machine (FRITSCH Pulverisette 7 premium line, Seoul National University). The crystalline SiO_2 powder (~600 mg) was loaded into a 20 mL ZrO_2 bowl with 24 ZrO_2 balls (diameter: 5 mm; total: ~9 g). Ball-milled SiO_2 with varying milling durations at 800 rpm was prepared by using a 20 mL ZrO_2 bowl with five ZrO_2 balls (8 mm in diameter). The SiO_2 powder was dried in a furnace at 300 °C for more than 12 h. The dried SiO_2 powder (of 200 mg) was ball-milled. The ball-to-powder weight ratio (BPR) was approximately 40 : 1. Ball milling was performed for 10 min and then rested for 10 min to minimize heating. Ball milling was performed at milling durations of 10, 20, 30, 60, 120, and 180 min at 800 rpm. To observe the oxygen bonding configurations *via* ^{17}O MAS NMR, ~100 mg of ^{17}O-enriched (40%) amorphous SiO_2 (ref. 50) was ball-milled by applying a 20 mL ZrO_2 bowl, five ZrO_2 balls (8 mm in diameter; BPR of ~80 : 1), and a milling speed of 800 rpm for 15 and 60 min. We also synthesized 40% ^{17}O-enriched crystalline SiO_2 from melting at 1500 °C for 2 h using 40% ^{17}O-enriched

amorphous SiO_2, which resulted in forming the crystalline SiO_2 (cristobalite) phase. Then, ~90 mg of ^{17}O-enriched (40%) c-SiO_2 (cristobalite) was ball-milled by applying a 20 mL ZrO_2 bowl, five ZrO_2 balls (8 mm in diameter; BPR of ~90 : 1), and a milling speed of 800 rpm for 15 and 60 min. We note that ^{17}O-enriched a-SiO_2 of ~100 mg and ^{17}O-enriched c-SiO_2 (cristobalite) of ~90 mg were milled with milling durations of 15 and 60 min, respectively.

2.2. XRD & high-resolution TEM

X-ray diffraction (XRD) experiments were performed by using a Rigaku MiniFlex 600 with Cu Kα emission with a wavelength of 1.5406 Å (Seoul National University). In continuous mode with a scan speed of 2.5° min^{-1}, we acquired the XRD pattern at 2θ intervals of 0.02° from 5 to 90° at 40 kV and 15 mA. High-resolution transmission electron microscopy (HRTEM) with energy-dispersive X-ray spectroscopy (EDS) was used to examine the morphologies and chemical composition of the SiO_2 milled in our planetary ball-milling system.

2.3. FT-IR spectroscopy

We collected the Fourier transform infrared (FT-IR) spectra for the milled oxides using a TENSOR27 spectrometer (Seoul National University) with a spectral resolution of 4 cm^{-1}. The spectral range spans from 400 to 4000 cm^{-1}. The scans were collected 32 times in attenuated total reflectance mode by using a mid-IR source. A diamond crystal plate was used to place a few milligrams of each sample in the optical window.

2.4. NMR spectroscopy

A Varian 9.4 T (400 MHz) NMR spectrometer was used for acquiring the ^{29}Si MAS NMR spectra with a ^{29}Si Larmor frequency of 79.47 MHz (Seoul National University). A Doty 4 mm probe was used with a spinning speed of 11–12 kHz (12 kHz for the milled SiO_2 from 200 to 800 rpm for 5 h, and 11 kHz for those deformed at a milling speed of 800 rpm with varying milling durations ranging from 10 to 180 min). The ^{29}Si MAS NMR spectra were acquired using a ~30° pulse (1.6 μs) with varying recycle delays. ^{1}H MAS NMR spectra at a spinning speed of 20 kHz, ^{29}Si MAS NMR spectra of 7 nm amorphous silica, 40% ^{17}O-enriched a-SiO_2 and ^{17}O-enriched c-SiO_2 (before and after milling at 800 rpm) at a spinning speed of 15 kHz (~30° pulse of 1 μs with a recycle delay of 10 s), and ^{1}H–^{29}Si Lee-Goldburg cross-polarization HetCor NMR spectra with a contact time of 3 ms and a rotor spinning rate of 15 kHz were recorded on a Bruker 14.1 T (600 MHz) NMR spectrometer and a Bruker 3.2 mm probe (Seoul National University). Tetramethylsilane (TMS) was the external standard for ^{29}Si and ^{1}H NMR chemical shifts. To ensure complete relaxation, ^{1}H MAS NMR spectra were collected with recycle delays exceeding 5 times spin-lattice relaxation time (T_1)[51] (see ESI-1†). Long recycle delays of ≥30 s with a 90° pulse (2.5 μs) were used for SiO_2 deformed at 800 rpm with varying milling durations. To obtain the ^{1}H MAS NMR spectra, the NMR signals of ball-milled SiO_2 were subtracted from the background spectrum of the empty rotor. Adamantane ($C_{10}H_{16}$) was used as the standard to estimate the hydrogen contents.[52] ^{17}O MAS NMR spectra were recorded on a Bruker 14.1 T (600 MHz) NMR spectrometer with a ^{17}O Larmor frequency of 81.39 MHz and a Bruker 3.2 mm probe with a rotor spinning speed of 20 kHz. ^{17}O MAS NMR spectra were obtained with a recycle delay of 1 s and a pulse length of ~0.2 μs. Tap water was used as the external standard. Here, we reported the ^{17}O MAS NMR spectrum of 40% ^{17}O-enriched amorphous SiO_2 and also 40% ^{17}O-enriched c-SiO_2 (cristobalite). Because of the low natural abundance of ^{17}O (0.037%), currently, it is challenging to obtain the ^{17}O NMR spectrum for natural abundance a-SiO_2. Note that ESI-1† describes the detailed spectroscopic and synthesis conditions.

3. Results and discussion

3.1. Mechanical amorphization of SiO_2 *via* mechanical milling: XRD, TEM-EDS, and FT-IR analysis

3.1.1 XRD. Fig. 1a shows the XRD patterns of SiO_2 under mechanical shear with varying milling speeds up to 800 rpm. The XRD patterns indicate a decrease in the peak intensities of c-SiO_2 above ~400 rpm, with a significant decrease at ~27° [(101) of quartz]. A broad feature spanning between 15° and 35° emerged above ~600 rpm, indicating the formation of the milled amorphous silica product. Above ~400 rpm, an additional peak was observed at ~30°; it has been attributed to the (111) peak of tetragonal ZrO_2, confirming the occurrence of ZrO_2 media wear during milling. The intensity of the ZrO_2 peak (at ~30°) increases with increasing milling speed, indicating an increase in the attrition of the ZrO_2 media at higher milling speeds. Indeed, the measured weight losses of the ZrO_2 balls during the 5 h milling of 600 mg of SiO_2 were ~60 and ~110 mg at 600 and 800 rpm, respectively (see ref. 32 for more details). Notably, increasing the milling time and speed resulted in higher degrees of ball wear. Meanwhile, the absence of zircon ($ZrSiO_4$) in the XRD patterns indicates that the current ball-milling did not provide sufficient energy to form such a crystalline compound, as the synthesis of zircon from its precursors typically requires a high temperature of ~1600 °C.[53]

3.1.2 TEM-EDS and FT-IR. Fig. 1b shows the TEM-EDS results for the mechanically deformed SiO_2 milled at 600 rpm. The TEM-EDS results reveal ZrO_2 particles of ~100 nm in size (circle in Fig. 1b(A)), confirming the wear of the milling media during the mechanical deformation of SiO_2. The EDS map of Zr (Fig. 1b(E)) also confirms that Zr is well dispersed throughout the milled amorphous silica product particles. The typical size of unmilled c-SiO_2 is a few hundred μm. The TEM images of milled SiO_2 at 600 rpm (Fig. 1b) and SEM images of milled SiO_2 at 800 rpm reveal a particle size of ~100–200 nm.[32] The particle size decreases and the surface area increases with increasing milling speed. Fig. 1c presents the FT-IR spectra of SiO_2 for various milling speeds. The quartz peak and a shoulder peak are, respectively, shown at ~1080 and ~1160 cm^{-1}, which correspond to the transverse and longitudinal optical modes for the asymmetric Si–O–Si stretching vibration, respectively; the peaks at ~800 (labelled as A) and ~700 cm^{-1} (B) correspond to the symmetric Si–O stretching and Si–O–Si bending vibrations.[49,54,55] At a milling speed of ~200 rpm, the IR feature at

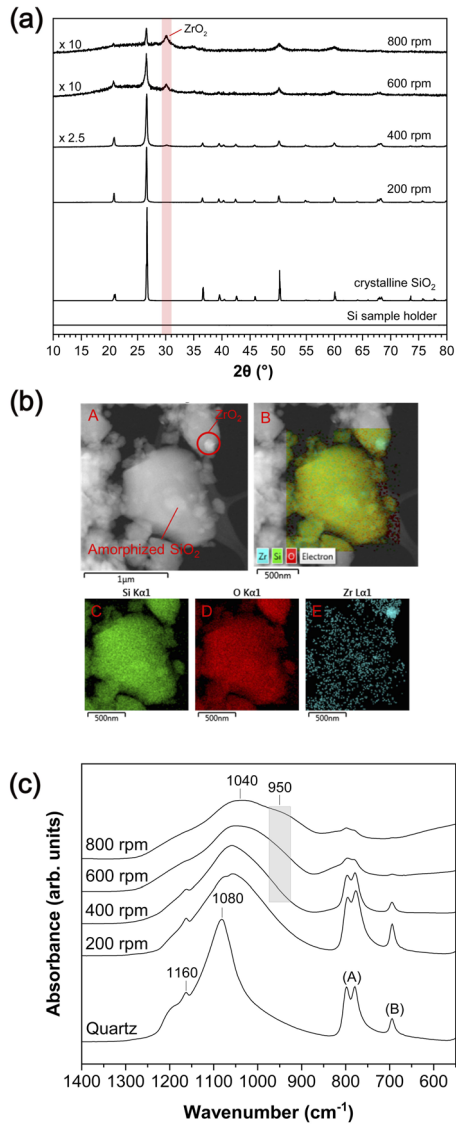

Fig. 1 (a) X-ray diffraction patterns for milled SiO_2 with varying milling speeds for 5 h. The XRD pattern of the sample holder is also shown. (b) TEM images for milled SiO_2 with a milling speed of 600 rpm for 5 h (red A and B) and EDS mapping for Si (red C), O (red D) and Zr elements (red E). (c) FT-IR spectra for milled SiO_2 with varying milling speeds for 5 h.

$\sim$1080 cm^{-1} red-shifted to $\sim$1040 cm^{-1}, potentially owing to the stress-induced deformation of c-SiO_2; this may indicate a decrease in the Si–O–Si bond angle during milling,[56] partially attributed to an increase in the fraction of three-membered rings.[57] We also observed the quartz peak intensities to decrease with increasing milling speed, as well as the quartz features broadening slightly, implying a deformation-induced increase in the structural disorder in c-SiO_2.

Above $\sim$400 rpm, we observe an additional feature at $\sim$950 cm^{-1}, and its intensity increases with increasing milling speed up to $\sim$800 rpm. This feature may be primarily attributable to the Si–O–Zr bond,[55,58,59] indicating a chemical reaction between SiO_2 and ZrO_2 under the condition of milling above 400 rpm (see ESI-2 and Fig. S1†). Although this feature could also be attributable to Si–OH groups that can be expected at $\sim$980 cm^{-1},[60] the intensity of this feature did not decrease upon heating the milled SiO_2 up to 700 °C (see ESI-2†), which may have removed all potential hydroxyl groups.[37] These results demonstrate that the amorphized SiO_2 and worn ZrO_2 particles from the milling media interact to form new chemical bonds during mechanical amorphization.

3.2. Deformation-induced change in network connectivity in the milled amorphous silica product under frictional shear and the interaction with milling media: ^{17}O MAS NMR spectroscopy results

Fig. 2 shows the ^{17}O MAS NMR spectra of ^{17}O-enriched a-SiO_2 before and after milling at 800 rpm. The dominant peak at $\sim$75 to ~-25 ppm has been attributed to the Si–O–Si bonds, with an additional contribution from the Si–OH groups, whereas the features associated with Si–OH groups may not have fully resolved from the Si–O–Si bonds[24,49,61] (see also ^{1}H MAS NMR results below for further discussion on the effects of hydration). The spectral width of the Si–O–Si peak increases with prolonged milling duration (Fig. 2c), revealing an increase in the structural disorder and the extent of deformation.[48,62] The ^{17}O NMR spectrum of a-SiO_2 subjected to mechanical shearing reveals additional broad features at $\sim$100–230 ppm, and they are attributable to Si–O–Zr bonds.[49] Therefore, the ^{17}O NMR results provide direct evidence that the enhanced interactions between ZrO_2 and SiO_2 during the intense milling-induced amorphization process resulted in Si–O–Zr bond formation. Additionally, the intensity of the Si–O–Zr peak increases with prolonged milling duration, and the bond fraction of Si–O–Zr [*i.e.*, (Si–O–Zr)/(Si–O–Si + Si–O–Zr)] following 15 and 60 min of milling at 800 rpm are $\sim$4% and $\sim$9%, respectively (see Fig. S3†), confirming unequivocally that the degree of chemical interaction increases with increasing milling duration and amorphization (see ESI-4† for XRD, ^{1}H and ^{29}Si MAS NMR spectra).

The amorphous phase formed *via* an intense milling of crystalline SiO_2 during mechanical amorphization also consists of Si–OH; as shown from the ^{1}H and ^{29}Si spectra (Fig. S5 and S6†), OH is barely present in the ^{17}O-enriched a-SiO_2 before milling but is produced during milling. The amount of OH is comparable to the non-enriched SiO_2. An earlier experimental study of ^{17}O-labeled silica[24] revealed the formation of Si–OH under shorter milling durations of 5 and 15 min using a mixer mill with a frequency of 25 Hz. The current study is consistent with the earlier study. In addition to Si–OH, the current results reveal the formation of Si–O–Zr in SiO_2 under intense ball milling.

Fig. 2d shows the ^{17}O MAS NMR spectra for ^{17}O-enriched c-SiO_2 (cristobalite) with milling durations of 15 and 60 min at 800 rpm (see ESI-4† for ^{29}Si MAS NMR spectra, XRD and ^{1}H MAS NMR results). The dominant peak with a typical quadrupolar line shape at $\sim$50 to ~-25 ppm of ^{17}O-enriched c-SiO_2 (cristobalite) before milling has been assigned to the single bridging oxygen (BO) site from the Si–O–Si bonds.[63,64] The crystalline quadrupolar pattern for the Si–O–Si peak disappears and the spectral width increases after milling durations of 15 and 60 min. This confirms increases in the structural disorder and amorphization of SiO_2 cristobalite. The ^{17}O NMR spectrum of milled ^{17}O-enriched c-SiO_2 (cristobalite) also shows broad

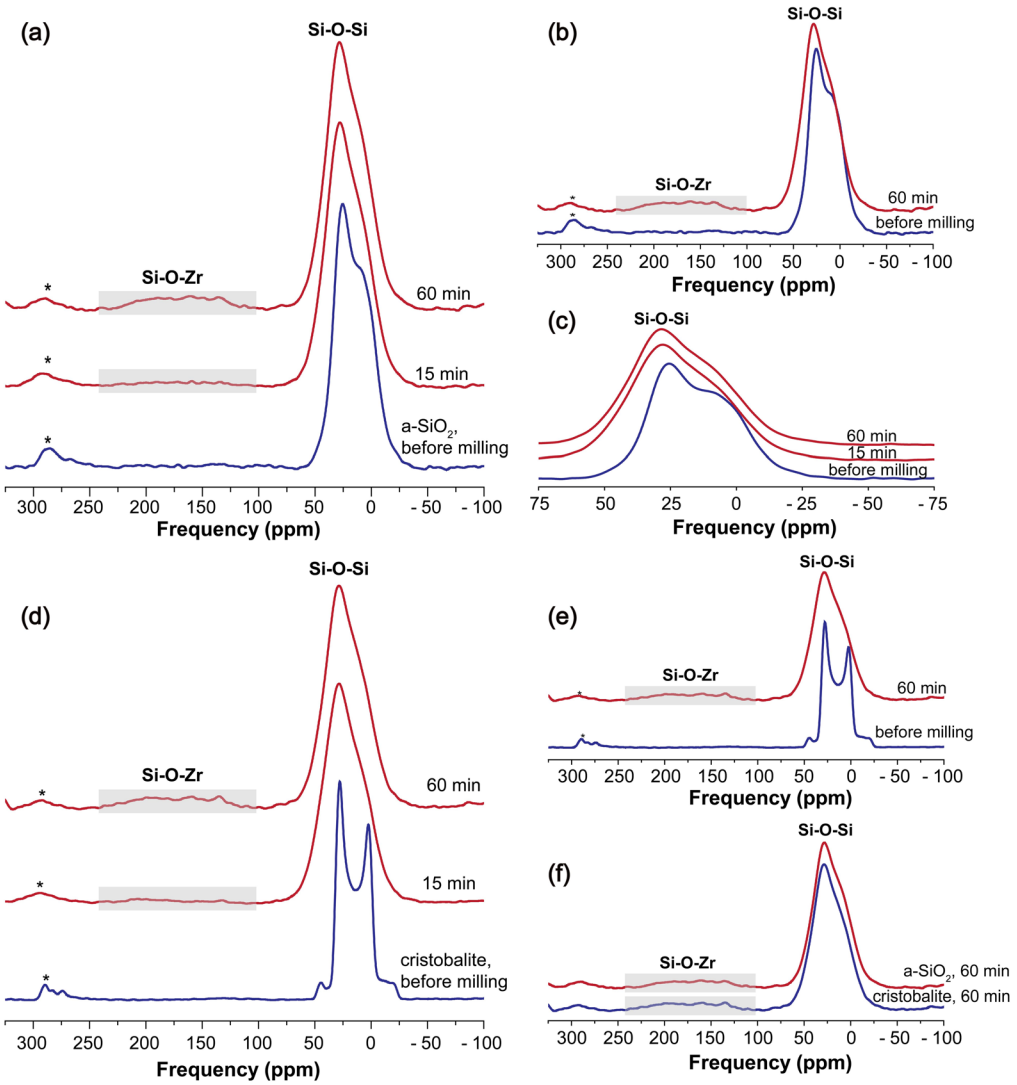

Fig. 2 (a) ^{17}O MAS NMR spectra with ^{17}O-enriched a-SiO_2 before and after milling at 800 rpm. The asterisks (*) indicate the spinning sidebands. (b) ^{17}O MAS NMR spectra of ^{17}O-enriched a-SiO_2 before and after milling of 60 min at 800 rpm. (c) Enlarged ^{17}O MAS NMR spectra between 75 ppm and −75 ppm for ^{17}O-enriched a-SiO_2 before and after milling at 800 rpm. (d) ^{17}O MAS NMR spectra with ^{17}O-enriched c-SiO_2 (cristobalite) before and after milling at 800 rpm. The asterisks (*) indicate the spinning sidebands. (e) ^{17}O MAS NMR spectra of ^{17}O-enriched c-SiO_2 (cristobalite) before and after milling of 60 min at 800 rpm. (f) ^{17}O MAS NMR spectra of ^{17}O-enriched c-SiO_2 (cristobalite) and ^{17}O-enriched a-SiO_2 after milling for 60 min at 800 rpm.

features at ∼100–230 ppm, which are due to Si–O–Zr bonds. The intensity of the Si–O–Zr peak also increases with increased milling duration, consistent with those observed from the milling-induced transitions in amorphous SiO_2 (Fig. 2a–c). The fractions of Si–O–Zr bonds in milled ^{17}O-enriched c-SiO_2 (cristobalite) with milling durations of 15 and 60 min at 800 rpm were ∼4% and ∼9% (Fig. 2d), respectively, which shows remarkable similarity to those of milled ^{17}O-enriched a-SiO_2 (Fig. 2a). After milling for 60 min at 800 rpm, the ^{17}O NMR spectra of ^{17}O-enriched c-SiO_2 (cristobalite) and ^{17}O-enriched a-SiO_2 are similar (Fig. 2f). The ^{17}O NMR results confirm that milling-induced amorphization is prevalent under a milling speed of 800 rpm and duration of 15 min with the formation of an extrinsic Si–O–Zr bond.

3.3. Mechanical milling-induced hydration of the milled amorphous silica product: hydrogen speciation and quantification of ^{1}H contents by ^{1}H MAS NMR analysis

3.3.1 ^{1}H MAS NMR analysis of SiO_2 under frictional shear with various milling speeds and durations. Fig. 3a shows the high-resolution ^{1}H MAS NMR spectra of SiO_2 subjected to mechanical shear at milling speeds of 200–800 rpm with a milling duration of 5 h. Multiple hydrogen species were identified, confirming the hydration and hydroxylation of SiO_2 after intense milling (see ref. 37 and the references therein for peak assignments; Fig. S11† for spectral deconvolution); particularly, a broad peak at ∼11 ppm indicates strongly hydrogen-bonded silanol, a broad peak at ∼6 ppm indicates moderately hydrogen-bonded silanol, a narrow peak at ∼4 ppm indicates weakly hydrogen-

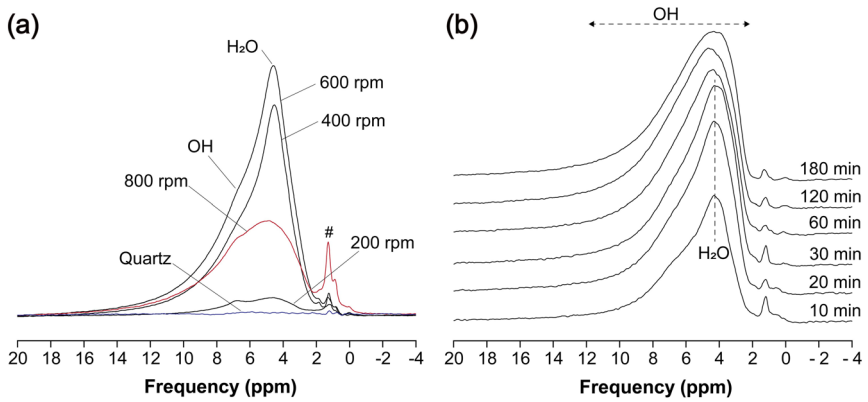

Fig. 3 (a) ^{1}H MAS NMR spectra (at 14.1 T) for milled SiO_2 with varying milling speeds using a milling duration of 5 h (the number of protons in the unit sample weight estimated from the spectral intensity).[37] The peak at ~1.3 ppm (#) is due to organic contamination such as finger grease.[67] (b) ^{1}H MAS NMR spectra (at 14.1 T) obtained for milled SiO_2 with varying milling durations at 800 rpm (the number of protons in the unit sample weight estimated from the spectral intensity).

bonded silanol and/or mainly hydrogen-bonded, surface-adsorbed water, and a narrow peak at ~4.7 ppm indicates surface-adsorbed water. The sharp peaks at ~1.2 ppm (# in Fig. 3a) are likely attributable to organic contamination. The broad peaks at ~6.4 and ~5.4 ppm may also indicate hydrogen-bonded water with varying hydrogen bond strengths.[37] The spectral intensity at 200 rpm is relatively weak, indicating minor hydration at lower milling speeds. The ^{1}H MAS NMR spectra obtained at 400 and 600 rpm reveal an increase in the peak intensities of the adsorbed H_2O and/or OH species. Under a much faster milling speed of 800 rpm, the spectral intensity and hydrogen content for the phase noticeably decrease, indicating the dehydration of the milled amorphous silica product at the elevated temperatures associated with intense milling at ~800 rpm;[65,66] these decreases primarily occurred at ~3–7 ppm (*i.e.*, adsorbed H_2O) (see ESI-6† for quantitative details).

The impact of the milling duration on the hydrogen environment of the milled amorphous silica product at a constant milling speed of 800 rpm is illustrated in Fig. 3b. The NMR results confirm an overall increase in the hydrogen content in the milled amorphous silica product with increasing milling duration and milling speed; this is because milling-induced comminution and a larger surface area tend to promote the hydration and hydroxylation of milled amorphous silica product surfaces. These results also indicate that, under rapid frictional shear and a relatively long milling duration (of 30 min under 800 rpm), frictional heating during such intense milling can also dehydrate and/or dehydroxylate the phase during amorphization.

3.4. Evolution of network structures of the milled amorphous silica product under frictional shear: insights from ^{29}Si MAS NMR analysis

3.4.1 Amorphous structures at varying milling speeds: ^{29}Si NMR results with a short recycle delay time. The atomic environments of the Si atoms in mechanically deformed SiO_2 are investigated by using ^{29}Si MAS NMR spectroscopy. Fig. 4a shows the ^{29}Si MAS NMR spectra of milled SiO_2 at speeds of up to 800 rpm with a milling duration of 5 h. The ^{29}Si MAS NMR spectra were obtained with a short NMR recycle delay of 10 s (Fig. 4a). Because the T_1 relaxation time of quartz is substantially longer than that of its amorphous analog, under a shorter NMR recycle delay time of 10 s, the signal from the amorphous component (milled amorphous silica product) is preferentially highlighted (see ref. 5 for further discussion). Even under such conditions, the spectrum at 200 rpm is dominated by a quartz resonance, indicating a minor degree of amorphization. Increasing the milling speed above ~400 rpm results in a broad peak ranging between ~−80 and ~−120 ppm, confirming the formation of the milled amorphous silica product. The ^{29}Si MAS NMR spectrum of unmilled a-SiO_2 shows a prominent feature at ~−110 ppm corresponding to fully polymerized Q^4 species.[37] However, at 600 and 800 rpm, the ^{29}Si MAS NMR spectra display apparent increases in their peak intensities, shifting toward higher frequency ranges (~−80 to ~−100 ppm). The changes reflect a milling-induced decrease in polymerization of the glass network (see discussion below). The milled SiO_2 exhibits Si–O–Zr and hydroxyl species (Si–O–H) along with growing structural disorder during amorphization and thus, we note again that the amorphous product formed by the amorphization of crystalline SiO_2 is not pure a-SiO_2.

3.4.2 Structural evolution at varying milling speeds: ^{29}Si NMR results with a long NMR recycle delay. Fig. 4b shows the ^{29}Si MAS NMR spectra with a relaxation delay of 4200 s for SiO_2 milled at varying milling speeds up to 800 rpm with a milling duration of 5 h, which resulted in fully relaxed ^{29}Si MAS NMR spectra for the milled SiO_2. Therefore, these ^{29}Si MAS NMR spectra obtained under a long relaxation delay provide quantitative information on both the crystalline (with long T_1) and amorphous phases (with short T_1). These results are consistent with XRD results (Fig. 1a). At 200 rpm, the ^{29}Si MAS NMR spectrum is again dominated by a strong quartz peak. At 400 rpm, the ^{29}Si MAS NMR spectrum indicates the dominance of quartz, which was partially observed with a short recycling delay of 10 s (Fig. 4a). As the milling speed increases, the broad peak intensity of milled amorphous silica product increases,

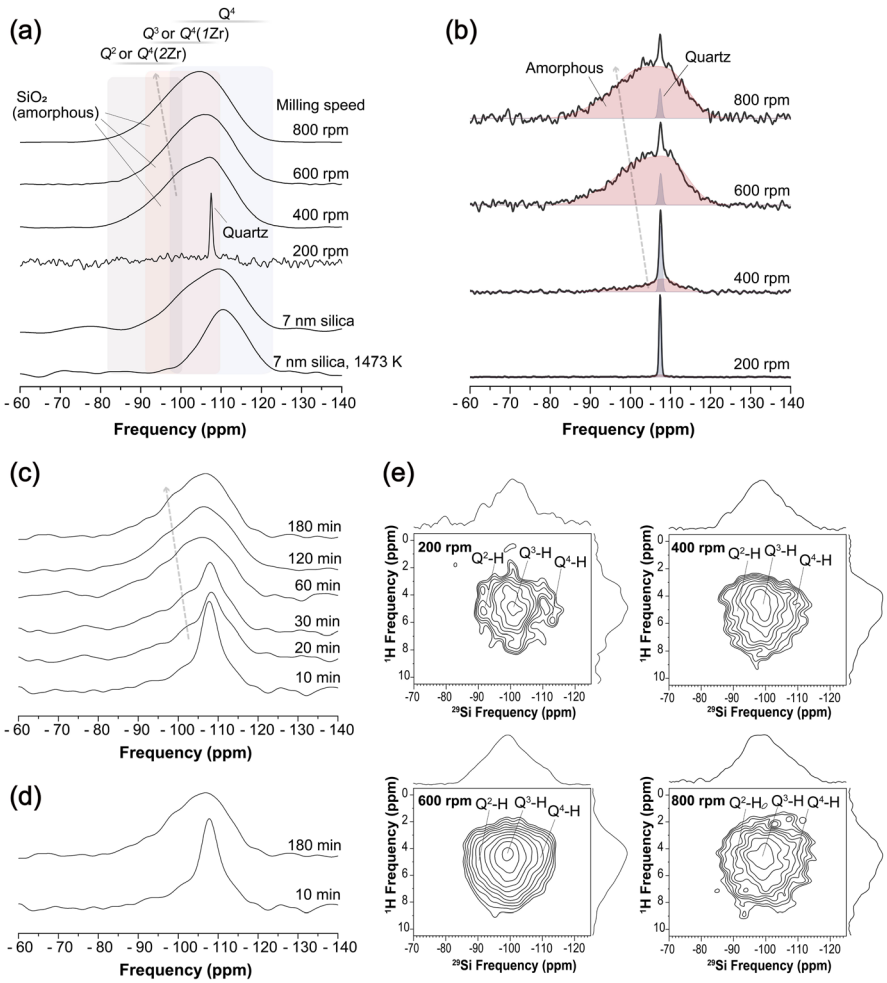

Fig. 4 (a) ^{29}Si MAS NMR spectra for milled SiO_2 with varying milling speeds with a milling duration of 5 h and 7 nm amorphous silica, the used recycle delay is 10 s. The ^{29}Si spectrum of 7 nm amorphous silica dehydrated at 1473 K was from the previous study.[37] (b) ^{29}Si MAS NMR spectra for milled SiO_2 with varying milling speeds with a milling duration of 5 h, the used recycle delay is 4200 s. (c) ^{29}Si MAS NMR spectra for milled SiO_2 with varying milling durations at 800 rpm, the used recycle delay is 3600 s (7200 s for the milled SiO_2 for 180 min). (d) ^{29}Si MAS NMR spectra for milled SiO_2 at 800 rpm with milling durations of 10 and 180 min. (e) ^{1}H–^{29}Si heteronuclear correlation (HetCor) NMR spectra and projections in ^{1}H and ^{29}Si dimensions for milled SiO_2 with varying milling speeds using a milling duration of 5 h.

confirming the milling-induced mechanical amorphization of quartz (Fig. 1a). While it is not fully quantitative, the residual c-SiO_2 was estimated to be ~ a few % based on the XRD peak area of the milled silicate at 800 rpm for 5 h (Fig. 1a), showing primarily the amorphous phase. The ^{29}Si NMR fraction of the milled amorphous silica product in the milled SiO_2 is ~97% (Fig. 4b), which is consistent with XRD results.

3.4.3 Structural evolution under varying milling durations: ^{29}Si MAS NMR results. Fig. 4c shows the relaxed ^{29}Si MAS NMR spectra for SiO_2 subjected to frictional shear under 800 rpm, milling durations ranging from 10 to 180 min, and a long NMR recycle delay (*i.e.*, 3600–7200 s). As the milling duration increases from 10 to 60 min, the fraction of c-SiO_2 decreases (see also Fig. S12† for XRD patterns). As for Fig. 4b, c-SiO_2 of ~600 mg was milled with varying milling speeds (from 200 to 800 rpm) for 5 h. As for Fig. 4c, c-SiO_2 of 200 mg was ground with varying milling durations (from 10 to 180 min) at 800 rpm. Considering the difference in sample volume, Fig. 4c presents a result for milled SiO_2 under more intense frictional shear. The spectral widths associated with the milled amorphous silica product also increase as a result of increasing the milling durations up to 60 min, suggesting an increase in the configurational and topological disorder within the amorphous network. Beyond 60 min, further increasing the milling duration to 180 min resulted in minor changes in the overall spectra. These results highlight that a time-dependent dynamic milling process occurred in the milled SiO_2, where network amorphization is controlled by tuning the milling speed and duration (Fig. 4d).

We also collected the ^{29}Si NMR spectra for ^{17}O-enriched crystalline SiO_2 (cristobalite) without milling and those with milling durations of 15 and 60 min under 800 rpm (Fig. S7†). The spectral results are compared to those of ^{17}O-enriched amorphous SiO_2 (Fig. S6–S8†). Using ^{17}O-enriched a-SiO_2 and ^{17}O-enriched c-SiO_2 (cristobalite) as starting materials, the ^{29}Si MAS NMR spectra for the milled amorphous phase are rather

similar, both showing an increase in peak intensity around ~−90 to ~−105 ppm (see Fig. S6–S8†). We note that with a short NMR recycle delay of 10 s used in the current ^{29}Si NMR spectral acquisition, the fraction of the crystalline peak is underestimated (see the section of Amorphous structures at varying milling speeds: ^{29}Si NMR results with a short recycle delay time above for further discussion). Nevertheless, the results confirm that the amorphous phases with different starting materials (*i.e.*, cristobalite and a-SiO_2) undergo similar amorphization paths, involving network depolymerization, hydroxylation, and the formation of extrinsic bonds resulting from interactions with the milling media.

3.4.4 Probing the hydroxylation of the milled amorphous silica product during milling: 2D ^{1}H–^{29}Si HetCor NMR results. Fig. 4e shows the 2D ^{1}H–^{29}Si HetCor NMR spectra for SiO_2 under frictional shear, revealing the spatial proximity between the hydrogen species (*e.g.*, hydrogen-bonded water and/or hydrogen-bonded silanol) and Q^n species in the milled amorphous silica product. The results reveal strong correlations for Q^2-H and Q^3-H (*i.e.*, through-bond and through-space correlations), whereas the correlation for Q^4-H is relatively weak. This suggests that the hydration of SiO_2 results in the formation of geminal silanol (Q^2) and single silanol (Q^3) (Fig. 3 and see also Fig. S13† for ^{1}H–^{29}Si CPMAS NMR spectra), which partially accounts for the high-frequency features (~−90 ppm) in the ^{29}Si MAS NMR spectra for the deformed SiO_2 under milling (Fig. 4a).

3.4.5 Structural origins of the milling-induced Q species evolution in the milled amorphous silica product subjected to mechanical amorphization. The broad spectral features of the amorphous component at −90 ppm (*i.e.*, deformation-induced peak shift from −110 ppm) of the mechanically amorphized SiO_2 may have multiple structural origins. First, as indicated by the FT-IR spectra in Fig. 1c and ^{17}O MAS NMR results in Fig. 2a, the shift originates from the formation of Si–O–Zr bonds. The observed interaction between ZrO_2 and SiO_2 leads to the formation of multiple Si environments with varying numbers of Zr atoms as second-nearest neighbors ($Q^4(m\mathrm{Zr})$, where m indicates the number of Zr atoms as the second-nearest neighbors of Si).[49,68,69] Given the estimated $X_{\mathrm{Si-O-Zr}}$ fraction of ~9% for SiO_2 milled at 800 rpm (Fig. 2), the $Q^4(m\mathrm{Zr})$ fractions with varying values of m can be estimated using the following equation:[70]

$$Q^4(m\mathrm{Zr}) = {}_4C_m(0.09)^m(0.91)^{4-m}, \text{ where } {}_4C_m = \frac{4!}{m!(4-m)!} \quad (1)$$

The estimated $Q^4(m\mathrm{Zr})$ fractions are as follows: Q^4(0Zr), ~0.69; Q^4(1Zr), ~0.27; Q^4(2Zr), ~0.04; and Q^4(3Zr), ~0.003. Because the chemical shifts of these peaks are higher than those for Q^4(0Zr) (*i.e.*, less negative peak position), the formation of $Q^4(m\mathrm{Zr})$ species accounts for the observed peak shift in the ^{29}Si MAS NMR spectra for the milled SiO_2 (see ESI-9 and Fig. S14b†). Second, an increase in network depolymerization due to hydroxylation of the milled amorphous silica product and, thus, the formation of Q^2 with germinal silanol [(Si–O)$_2$═Si═(OH)$_2$] and Q^3 with single silanol [(Si–O)$_3$≡Si–OH][37] may partially account for the residual intensity, as the spectral patterns may not be fully explained by the estimated $Q^4(m\mathrm{Zr})$ fractions alone (see ESI-9 and Fig. S14c†). Lastly, because the ^{29}Si NMR chemical shift increases with decreasing Si–O–Si bond angle (see ref. 37 and the references therein), the current positive shift indicates a deformation-induced decrease in the Si–O–Si bond angles, as also implied by the FT-IR results (see ESI-10 and Fig. S15†).

To further identify the relative contributions of both Zr and H to Si speciation (*i.e.*, Q^2(2OH), Q^3(1OH), Q^4, and $Q^4(m\mathrm{Zr})$ species), the fractions of Q^n species in the amorphous phase were estimated by deconvoluting the ^{29}Si MAS NMR spectra collected under longer NMR recycle delays (see ESI-11 and ESI-12† for the effects of NMR relaxation time on quantification; ESI-13† for the effects of 10 and 4200 s recycle delays on the ^{29}Si MAS NMR spectra). Here, we first constrained the Q^4 peak position to ~−110 ppm based on the NMR signal of pure SiO_2 glass only with Q^4 species (Fig. 4a). The relative $Q^4(m\mathrm{Zr})$ proportions were then estimated based on the Si–O–Zr fraction from ^{17}O NMR (eqn (1)). The Q^4(2Zr) and Q^4(1Zr) peak positions were constrained to ~−92 and ~−101 ppm (ESI-9 and Fig. S14b†), with the relative intensities set to match the Q^4(2Zr), Q^4(1Zr), and Q^4 [*i.e.*, Q^4(0Zr)] ratios of approximately 4%, 27%, and 69%, respectively. Additionally, the residual spectral intensities of the experimental ^{29}Si MAS NMR signals have been attributed to the combination of Q^2 and Q^3 species at ~−92 and ~−101 ppm, respectively, accounting for the hydroxylation-induced changes in the Si species (see ESI-9 and Fig. S14c†). The fractions of Si species resulting from SiO_2 being subjected to frictional shear at 800 rpm were as follows: Q^2, 10%; Q^3, 24%; Q^4, 45%; Q^4(1Zr), 18%; and Q^4(2Zr), 3%. Although the Q^4 peak position was fixed at approximately −110 ppm, the potential positive peak shift in Q^4 could contribute to increase the fractions of Q^4 species, particularly the Q^4(1Zr) and Q^4(2Zr) species. Additionally, the fraction of Si–O–Zr bonds may be slightly underestimated because the Si–O–H bonds overlapped with the Si–O–Si bonds in the ^{17}O MAS NMR spectra (Fig. 2). Therefore, the current simulation results represent a conservative estimation of the fractions of Q^4(0Zr), Q^4(1Zr), and Q^4(2Zr) species in SiO_2 (see ESI-9† for further details and uncertainties).

Furthermore, although the effects of Si–O–Si bond angle reduction during deformation have not been explicitly considered, the systematic peak shift in the Q^4 species (toward a more positive frequency) can potentially provide quantitative insight into deformation-induced topological contraction (see Fig. S19† for milling-driven ^{29}Si peak shift). Regardless of this uncertainty, the current ^{29}Si results clearly highlight diverse deformation processes during milling, such as milling-induced chemical interactions, hydroxylation, and potential topological contraction (*i.e.*, bond-angle change) in SiO_2 networks during amorphization.

3.5. Quantification of the degree of amorphization in SiO_2 under mechanical shear

3.5.1 ^{29}Si MAS NMR results for SiO_2 milled at 800 rpm under varying milling durations and NMR recycle delays. The aforementioned results indicate that our NMR results for a longer NMR recycle delay can quantify the fractions of

crystalline and amorphous phases in intensely deformed SiO_2 subjected to mechanical amorphization. Here, based on our detailed, systematic, and extensive solid-state NMR results, we quantified the extent of SiO_2 amorphization during frictional slip by varying the milling speed and duration. Fig. 5a shows the ^{29}Si MAS NMR spectra for SiO_2 that underwent mechanical amorphization at 800 rpm with varying NMR recycle delays and milling durations. First, the ^{29}Si MAS NMR spectra confirmed that increasing NMR recycle delay can better highlight the crystalline quartz peak intensity at ~−107.5 ppm (see ESI-15†), demonstrating the necessity of collecting NMR spectra with long recycle delay for quantitative analyses. Second, increasing milling duration to 30 min results in broader and weaker c-SiO_2 spectral features, indicating enhanced structural disorder *via* mechanical milling. After ~60 min of milling, the crystalline signals disappear, even under a long recycle delay of 3600 s, confirming the absence of the crystalline phase and their complete conversion into the milled amorphous silica product (see ESI-16† for further details).

In Fig. 5b, the milling-driven evolution of ^{29}Si MAS NMR spectra for SiO_2 under distinct NMR recycle delays (10, 300, and 3600 s) is shown, which were used to determine the optimal NMR conditions for quantification of the NMR spectral features. The normalized spectra (Fig. 5b, right) show that the spectral intensities within the higher frequency range of −80 to −100 ppm are more prominent under the shorter recycle delay of 10 s. This is because the deformation-induced changes in the species with shorter T_1 relaxation times, such as Q^2, Q^3, Q^4(1Zr), and Q^4(2Zr), are more pronounced under the shorter NMR recycle delay; the electron spin resonance spectra (see ESI-12 and Fig. S17†) reveal an increase in the concentration of radical species (*i.e.*, unpaired electron spins) with increasing milling duration,[71] which reduces the T_1 relaxation times of the milled SiO_2. Our ESR spectra reveal the peroxy radicals, which originates from the increased contact of SiO_2 particles with the air (or oxidation) during milling. Furthermore, the reduced oxidation may preserve the E′ center and/or non-bridging oxygen hole center (NBOHC) (ESI-12† for further details).[72] This increase also indicates that the NMR relaxation delay time for the acquisition of the quantitative spectrum can be shortened (ESI-12†). Taking these factors into consideration, it is concluded that an NMR recycle delay of ≥3600 s provides the fully quantitative ^{29}Si MAS NMR spectra, enabling robust estimation of the Q^n and/or $Q^4(m\text{Zr})$ species in milled SiO_2 (see ESI-17† for further details).

3.5.2 Quantification of the milled amorphous silica product in milled SiO_2. We note that the quantification of the fractions of c-SiO_2 and the milled amorphous silica product is typically challenging *via* experimental probes such as XRD, Raman spectroscopy, and X-ray spectroscopy. Meanwhile, in the current study, deconvolution of the fully relaxed ^{29}Si MAS NMR spectra allows us to provide quantitative estimation of the

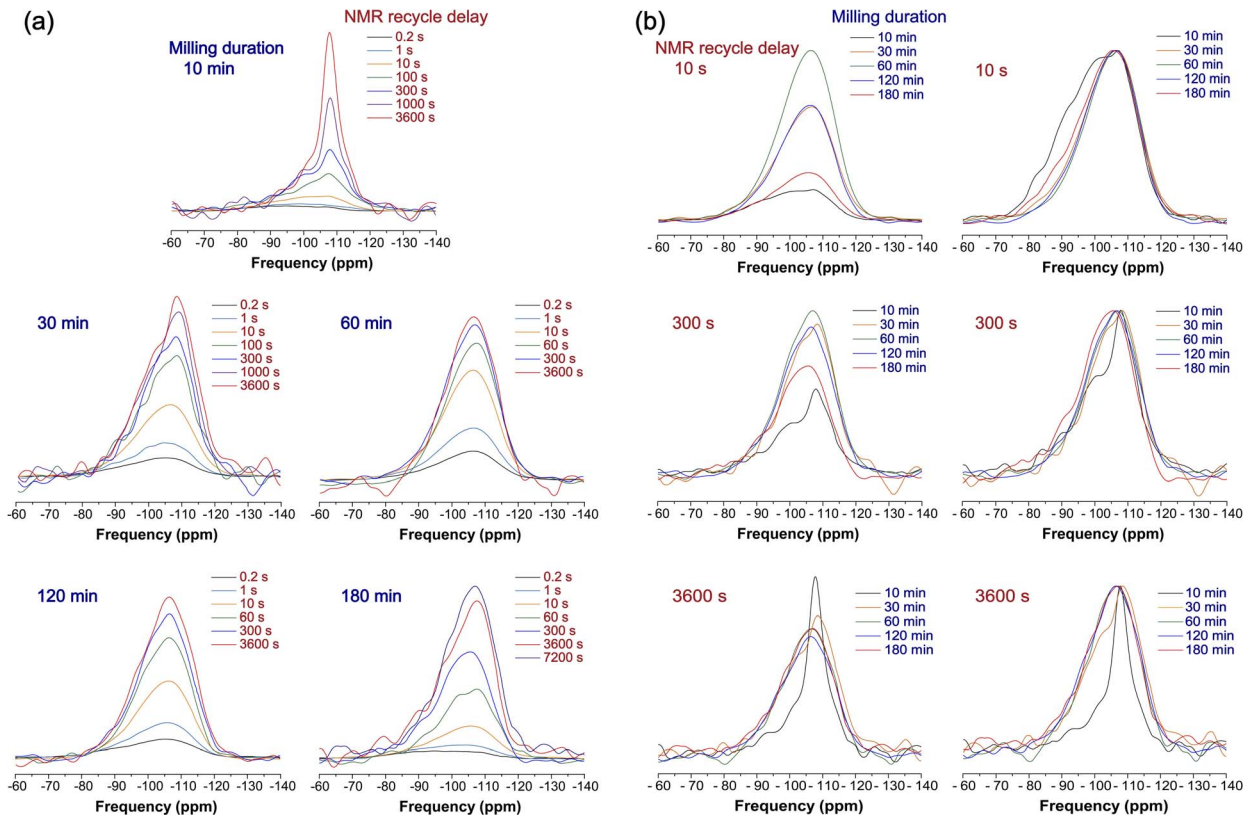

Fig. 5 (a) ^{29}Si MAS NMR spectra with varying NMR recycle delays (dark red) for milled SiO_2 at 800 rpm with varying milling durations (dark blue) from 10 to 180 min. (b) ^{29}Si MAS NMR spectra with varying NMR recycle delays (dark red) of 10, 300, and 3600 s for 10 to 120 min and 7200 s for 180 min for milled SiO_2 at 800 rpm with varying milling durations (dark blue) from 10 to 180 min (right: normalized spectra).

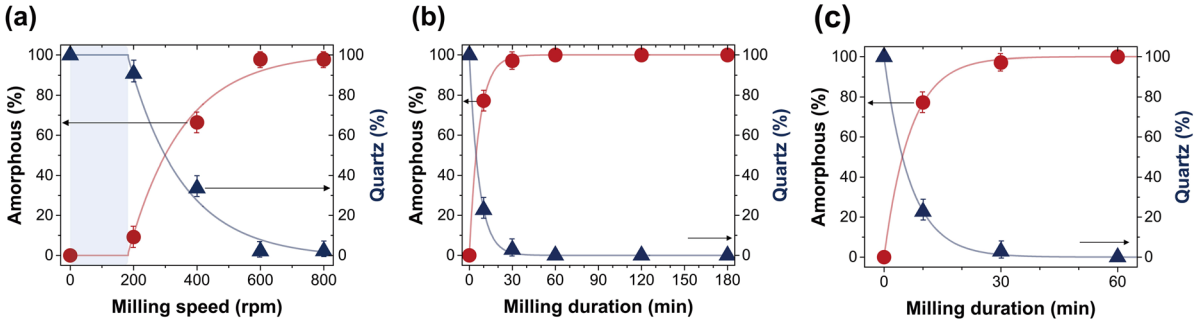

Fig. 6 (a) Variation in the fractions of crystalline SiO_2 and the milled amorphous silica product with varying milling speeds with a milling duration of 5 h, the used recycle delay is 4200 s. The solid lines show the shifted exponential function to model the fractions of c-SiO_2 and milled amorphous silica product upon increase in the milling speeds, revealing the threshold milling speed of ~185 rpm. The blue box indicates that the mechanical amorphization could not be achieved at milling speeds below ~185 rpm. (b) Variation in the fractions of crystalline SiO_2 and the milled amorphous silica product with varying milling durations at 800 rpm, the used recycle delay is 3600 s for 10 to 120 min and 7200 s for 180 min. The solid lines were fitted by a single exponential function. (c) Enlarged variation in the fractions for 10 to 60 min.

proportions of c-SiO_2 and the milled amorphous silica product. In particular, Fig. 6a reveals that the fraction of the milled amorphous silica product increases from ~10% at 200 rpm to ~67% at 400 rpm, and to ~97% at 600 and 800 rpm. The NMR results show that the mechanical amorphization of SiO_2 is most prominent within the milling-speed range from 200 to 600 rpm. Here, we use the shifted exponential function (dashed lines in Fig. 6a) to effectively model the milling-induced amorphization of SiO_2: $A(R) = A_0[1 - \exp(-(R - R_a)/\lambda_1)]$, where $A(R)$ is the amorphous fraction at varying milling speeds (R) and A_0 is the saturated amorphous fraction. The minimum milling speed (R_a) was also estimated to be ~185 rpm, and λ_1 was set to ~174 rpm; therefore, milling speeds below ~185 rpm cannot provide sufficient energy to activate mechanical amorphization and thus, the amorphization of SiO_2 can only be achieved above the threshold milling speed.

Fig. 6b and c illustrate the relationship between c-SiO_2 and milled amorphous silica product fractions and milling duration at 800 rpm. The fraction of the milled amorphous silica product sharply increased with increasing milling duration up to approximately 30 min. The fractions of the milled amorphous silica product were clearly saturated for milling durations above ~30 min. The relationship between milled amorphous silica product fraction and milling duration can also be explained using a single exponential function: $A(t) = A_0[1 - \exp(-t/D_1)]$, where $A(t)$ is the amorphous fraction for various milling durations and A_0 is the saturated amorphous fraction. The mechanical amorphization time, D_1, is defined as the milling duration required for the amorphization of ~63% of c-SiO_2. Under the current milling conditions, D_1 was estimated to be ~7 min. Although the extent of ball milling-induced mechanical amorphization had remained unknown, the current experimental results provide the first quantitative information on the fractions of crystalline and amorphous components in SiO_2 milled under varying speeds and durations. The extensive ^{29}Si NMR results, in conjunction with the inputs from the ^{17}O and ^{1}H results, enable us to establish the first predictive models for mechanical amorphization during intense milling.

3.6. Implications and applications

Our current results provide guidelines for controlling the structural disorder and fractions of crystalline–amorphous phases by tuning the milling speed and duration, and can be practically useful as novel mechanical milling-based synthesis protocols. Here, we discuss the implications further and the practical aspects of the current experimental findings and conceptual advances.

3.6.1 Formation of intrinsic and extrinsic chemical bonds during milling-driven amorphization. We have shown the extent of mechanical alloying of Zr and, therefore, the substantial degree of interaction between SiO_2 and milling media. In particular, while the formation of such extrinsic chemical bonds during mechanical milling had been difficult to probe, the current ^{17}O MAS NMR results provide unequivocal experimental evidence for the formation of Si–O–Zr bonds during milling. The observed milling-induced formation of Si–O–Zr may affect the physical properties of SiO_2. Indeed, earlier studies of sol–gel synthesized SiO_2–ZrO_2, a potential Li-ion battery anode material, have suggested that the formation of Si–O–Zr bonds enhances the specific capacity.[29,30] As ball-milling can be used to synthesize amorphous anode materials for energy storage, considering our current observation of milling-induced formation of Si–O–Zr, potential change (or enhancement) of capacity may also be due to the formation of extrinsic bonds (*via* interaction with milling media); whereas mechanosynthesis and the formation of intrinsic bonds (*i.e.*, without interacting with milling media) *via* ball-milling have been demonstrated extensively,[19,31] the current results also reveal the formation of extrinsic bonds. Such extrinsic bond formation may have partly contributed to an enhanced specific capacity of milled SiO_2 synthesized by mechanical milling.[28] Future studies and application of mechanochemical synthesis of anode materials should take the formation of such extrinsic chemical bonds into consideration. Alternatively, the formation of such bonds can in turn be used to chemically dope minor elements into oxide materials with substantial hardness (*e.g.*, SiO_2 and Al_2O_3) by controlling the overall degree of milling

speeds and durations. Such protocols may offer a novel synthesis method for amorphous materials with tunable electronic-transport properties.

3.6.2 Implications for frictional processes in natural systems. Our study also revealed the extensive mechanical amorphization-mediated hydration (~10% hydrogen atoms per SiO_2 unit), hydroxylation (*i.e.*, the formation of Si–O–H), and the subsequent depolymerization of the amorphous networks in the milled amorphous silica product. Because quartz (SiO_2) is a major mineral phase of the Earth's crust, the current experimental findings during mechanical amorphization of SiO_2 provide insight into the friction processes in nature. One of the salient examples is the friction processes of quartz and other silicate minerals on fault planes during co-seismic slip. In particular, as confirmed in the current study, frictional shear is expected to hydrate anhydrous SiO_2-rich minerals. Such hydration and hydroxylation could decrease the melting temperature of the minerals, promoting melt formation during rapid frictional slip (*i.e.* frictional melting) (see ref. 5 and references therein), which reduces the friction coefficient along the fault plane. The decrease in the friction coefficient due to melt lubrication of the fault surfaces accounts for an efficient slip. Therefore, although a direct comparison between the milling speeds of the planetary ball milling in our experiments and fault slip speed during an earthquake remains to be explored, our experimental finding can be useful to constrain the behaviors of SiO_2-rich minerals under extreme friction and provide atomistic account to facilitate longer displacement during slip.

3.6.3 Implications for amorphization during material processing under shear. We note again that "amorphization" of crystalline silica is accompanied by the formation of silanol and also Zr–O–Si, along with depolymerized Q^3 and Q^2 species, thereby presenting evidence of hydroxylation. Therefore, the amorphous products formed *via* intense milling are not pure a-SiO_2, rather an amorphous phase consisting also of a minor fraction of H and Zr. The current study explicitly reveals such transitions and formation of extrinsic bonds under intense milling. Furthermore, as can be inferred from the formation of Si–O–Zr and Si–O–H bonds in the mechanically milled amorphous silica product, extreme friction may activate chemical interactions among the materials under intense milling, which may reduce the melting temperature of the crystalline oxides. The current results suggest that the slip-softening mechanisms associated with frictional shear may also be activated above a specific threshold sliding speed. Finally, our study established the kinetic models for dynamic mechanical amorphization; quantification of the proportions of c-SiO_2 and the milled amorphous silica product by ^{29}Si MAS NMR allowed us to construct the kinetic paths of the irreversible mechanical amorphization. The established model identifies the threshold milling speed and duration (and thus, the energy barrier to activate the mechanical amorphization) to achieve the amorphization of SiO_2. The exponential model for the proportions of c-SiO_2 and the milled amorphous silica product reveals that the mechanical amorphization during intense-milling can be described as the first-order reaction. The current model, for the first time, defines the dynamic paths of the irreversible mechanical milling. Furthermore, the model provides the guidelines for novel mechanical-based synthesis routes for amorphous materials.

4. Conclusions

In the current study, we investigated extensively the extent of network amorphization of prototypical SiO_2 during intense milling and revealed the substantial degree of hydration, hydroxylation, and chemical interactions with the milling media at varying milling speeds and durations *via* multinuclear (^{1}H, ^{17}O, and ^{29}Si) NMR spectroscopy, together with XRD, TEM-EDS, and FT-IR. The current results constitute a full-spectrum analysis of the mechanical amorphization-driven structural evolution and interactions during milling, which has not been previously reported. Notably, as the milling speed and duration increase, the crystallinity of SiO_2 gradually decreased and it became amorphous. During milling-driven mechanical amorphization, the high-resolution ^{17}O NMR revealed the formation of Si–O–Zr bonds through the interaction of SiO_2 with ZrO_2 milling media. The ^{1}H NMR results also confirmed the hydration of the amorphous SiO_2 complex through the formation of Si–O–H species. The fully relaxed ^{29}Si MAS NMR spectra were used to quantify the fractions of c-SiO_2 and amorphous SiO_2 phase consisting of a hydroxyl group and Si–O–Zr at varying milling speeds and durations. The quantification of the fraction of the milled amorphous silica product revealed a threshold milling speed and duration. These findings help to explain the atomistic structural changes resulting from applying a ball-milling process to diverse materials with comparatively high hardness. Furthermore, our findings regarding deformation-induced chemical interactions and hydration also provide insight into structural changes in silicate rocks and melts during natural frictional processes (*e.g.*, fault slip). The amorphous product obtained *via* mechanical amorphization of c-SiO_2 has potential as an anode material for batteries and other energy storage materials. Future studies on comprehensive investigation of the formation of extrinsic and intrinsic chemical bonds for complex materials are needed. Our experimental findings provide guidelines for novel mechanical deformation-based synthesis routes for amorphous materials.

Data availability

The data supporting this article have been included as part of the ESI.†

Author contributions

Jin Jung Kweon: data curation, formal analysis, investigation, validation, visualization, writing – original draft, review & editing; Hoon Khim: data curation, formal analysis, investigation, visualization; Yong-Hyun Kim: writing – review & editing; Sung Keun Lee: conceptualization, formal analysis, methodology, funding acquisition, supervision, writing – original draft, review & editing.

Conflicts of interest

There are no conflicts of interest to declare.

Acknowledgements

This work was supported by the National Research Foundation of Korea (NRF) grant funded by the Ministry of Science and ICT to S. K. Lee. (2020R1A3B2079815). We are grateful to Prof. Seung Mo Oh and Dr Jae Gil Lee of the School of Chemical and Biological Engineering, Seoul National University for their discussion on synthesizing amorphous anode materials in July 2013. We thank Dr Jeongjae Lee for suggestions and editing of the earlier version of the manuscript.

References

1 A.-M. El-Sayed, Y. Wimmer, W. Goes, T. Grasser, V. V. Afanas'ev and A. L. Shluger, *Phys. Rev. B:Condens. Matter Mater. Phys.*, 2015, **92**, 014107.
2 K. Möller and T. Bein, *Chem. Mater.*, 2016, **29**, 371–388.
3 F. F. E. Kohle, J. A. Hinckley, S. Li, N. Dhawan, W. P. Katt, J. A. Erstling, U. Werner-Zwanziger, J. Zwanziger, R. A. Cerione and U. B. Wiesner, *Adv. Mater.*, 2019, **31**, 1806993.
4 A. A. Nayl, A. I. Abd-Elhamid, A. A. Aly and S. Brase, *RSC Adv.*, 2022, **12**, 13706–13726.
5 S. K. Lee, R. Han, E. J. Kim, G. Y. Jeong, H. Khim and T. Hirose, *Nat. Geosci.*, 2017, **10**, 436–441.
6 V. Samae, P. Cordier, S. Demouchy, C. Bollinger, J. Gasc, S. Koizumi, A. Mussi, D. Schryvers and H. Idrissi, *Nature*, 2021, **591**, 82–86.
7 N. Watanabe, H. Abe, A. Okamoto, K. Nakamura and T. Komai, *Sci. Rep.*, 2021, **11**, 5340.
8 Y. Wang, K. Xie, X. Guo, W. Zhou, G. Song and S. Cheng, *New J. Chem.*, 2016, **40**, 8202–8205.
9 O. Verho, F. Gao, E. V. Johnston, W. Wan, A. Nagendiran, H. Zheng, J.-E. Bäckvall and X. Zou, *APL Mater.*, 2014, **2**, 113316.
10 V. G. Chandrashekhar, T. Senthamarai, R. G. Kadam, O. Malina, J. Kašlík, R. Zbořil, M. B. Gawande, R. V. Jagadeesh and M. Beller, *Nat. Catal.*, 2021, **5**, 20–29.
11 C. Barbé, J. Bartlett, L. Kong, K. Finnie, H. Q. Lin, M. Larkin, S. Calleja, A. Bush and G. Calleja, *Adv. Mater.*, 2004, **16**, 1959–1966.
12 K. K. Qian and R. H. Bogner, *J. Pharm. Sci.*, 2012, **101**, 444–463.
13 S.-G. Kang, W. Jeong, J. Paeng, H. Kim, E. Lee, G.-S. Park, S. Han, H. Nam Han and I.-S. Choi, *Mater. Today*, 2023, **66**, 62–71.
14 X. Hou, M. Zhang, J. Wang, S. Hu, X. Liu and Z. Shao, *J. Alloys Compd.*, 2015, **639**, 27–35.
15 V. Zarei, M. Mirzaasadi, A. Davarpanah, A. Nasiri, M. Valizadeh and M. J. S. Hosseini, *Processes*, 2021, **9**, 334.
16 H. N. Kim, J. W. Kim, B.-D. So, Y. Keehm, B. H. Lee and J. C. Kim, *Geosci. J.*, 2022, **26**, 703–713.
17 S. L. James, C. J. Adams, C. Bolm, D. Braga, P. Collier, T. Friscic, F. Grepioni, K. D. Harris, G. Hyett, W. Jones, A. Krebs, J. Mack, L. Maini, A. G. Orpen, I. P. Parkin, W. C. Shearouse, J. W. Steed and D. C. Waddell, *Chem. Soc. Rev.*, 2012, **41**, 413–447.
18 D. Tan and F. Garcia, *Chem. Soc. Rev.*, 2019, **48**, 2274–2292.
19 K. Y. Baek, W. Lee, J. Lee, J. Kim, H. Ahn, J. I. Kim, J. Kim, H. Lim, J. Shin, Y. J. Ko, H. D. Lee, R. H. Friend, T. W. Lee, J. Lee, K. Kang and T. Lee, *Nat. Commun.*, 2022, **13**, 4263.
20 G. Gorrasi and A. Sorrentino, *Green Chem.*, 2015, **17**, 2610–2625.
21 F. Delogu, G. Gorrasi and A. Sorrentino, *Prog. Mater. Sci.*, 2017, **86**, 75–126.
22 S. F. H. Lambregts, L. M. de Kort, F. Winkelmann, M. Felderhoff, P. Ngene, E. R. H. van Eck and A. P. M. Kentgens, *J. Phys. Chem. C*, 2024, **128**, 12186–12193.
23 C. H. Chen, E. Gaillard, F. Mentink-Vigier, K. Chen, Z. Gan, P. Gaveau, B. Rebiere, R. Berthelot, P. Florian, C. Bonhomme, M. E. Smith, T. X. Metro, B. Alonso and D. Laurencin, *Inorg. Chem.*, 2020, **59**, 13050–13066.
24 C. H. Chen, F. Mentink-Vigier, J. Trebosc, I. Goldberga, P. Gaveau, E. Thomassot, D. Iuga, M. E. Smith, K. Chen, Z. Gan, N. Fabregue, T. X. Metro, B. Alonso and D. Laurencin, *Chem.–Eur. J.*, 2021, **27**, 12574–12588.
25 A. F. Fuentes and L. Takacs, *J. Mater. Sci.*, 2012, **48**, 598–611.
26 S. Hwang, S. Gratz and L. Borchardt, *Chem. Commun.*, 2022, **58**, 1661–1671.
27 T. Yamamoto, S. Ashida, N. Inubuse, S. Shimizu, Y. Miura, T. Mizutani and K.-i. Saitow, *J. Mater. Chem. A*, 2024, **12**, 30906–30918.
28 W.-S. Chang, C.-M. Park, J.-H. Kim, Y.-U. Kim, G. Jeong and H.-J. Sohn, *Energy Environ. Sci.*, 2012, **5**, 6895–6899.
29 D. Choi and K.-L. Choy, *Electrochim. Acta*, 2016, **218**, 47–53.
30 D. Choi and K. Choy, *Dalton Trans.*, 2017, **46**, 14226–14233.
31 H. Kim, J. E. Lee, S.-M. Jo and S. Wooh, *ACS Sustain. Chem. Eng.*, 2022, **10**, 9679–9686.
32 J. J. Kweon, H. Khim and S. K. Lee, *Korean Journal of Mineralogy and Petrology*, 2023, **36**, 95–106.
33 P. F. M. de Oliveira, R. M. Torresi, F. Emmerling and P. H. C. Camargo, *J. Mater. Chem. A*, 2020, **8**, 16114–16141.
34 A. P. Yuda, P. Y. E. Koraag, F. Iskandar, H. S. Wasisto and A. Sumboja, *J. Mater. Chem. A*, 2021, **9**, 18906–18926.
35 G. Di Toro, R. Han, T. Hirose, N. De Paola, S. Nielsen, K. Mizoguchi, F. Ferri, M. Cocco and T. Shimamoto, *Nature*, 2011, **471**, 494–498.
36 T. Watanabe, T. Isobe and M. Senna, *J. Solid State Chem.*, 1997, **130**, 284–289.
37 H. N. Kim and S. K. Lee, *Geochim. Cosmochim. Acta*, 2013, **120**, 39–64.
38 J. Lee and S. K. Lee, *Acta Mater.*, 2022, **241**, 118413.
39 A. C. Lee and S. K. Lee, *Geochim. Cosmochim. Acta*, 2024, **370**, 199–218.
40 W. Yang, Z. Wang, J. Huang and Y. Jiang, *J. Phys. Chem. C*, 2021, **125**, 10179–10197.
41 J. J. Kweon, H.-I. Kim, S.-h. Lee, J. Kim and S. K. Lee, *Acta Mater.*, 2022, **226**, 117657.

42 N. Lopatik, A. De, S. Paasch, A. Schneemann and E. Brunner, *Phys. Chem. Chem. Phys.*, 2023, **25**, 30237–30245.
43 S. M. Chemtob, G. R. Rossman and J. F. Stebbins, *Am. Mineral.*, 2012, **97**, 203–211.
44 E. Lam, K. Larmier, P. Wolf, S. Tada, O. V. Safonova and C. Copéret, *J. Am. Chem. Soc.*, 2018, **140**, 10530–10535.
45 J. F. Stebbins and X. Xue, *Rev. Mineral. Geochem.*, 2014, **78**, 605–653.
46 S. K. Lee and S. Ryu, *J. Phys. Chem. Lett.*, 2018, **9**, 150–156.
47 S. K. Lee, K. Y. Mun, Y. H. Kim, J. Lhee, T. Okuchi and J. F. Lin, *J. Phys. Chem. Lett.*, 2020, **11**, 2917–2924.
48 S. K. Lee, J. L. Mosenfelder, S. Y. Park, A. C. Lee and P. D. Asimow, *Proc. Natl. Acad. Sci. U. S. A.*, 2020, **117**, 21938–21944.
49 D. M. Pickup, G. Mountjoy, G. W. Wallidge, R. J. Newport and M. E. Smith, *Phys. Chem. Chem. Phys.*, 1999, **1**, 2527–2533.
50 S. K. Lee and E. J. Kim, *J. Phys. Chem. C*, 2014, **119**, 748–756.
51 M. Avramovska, D. Freude, W. Schwieger, T. Fey, J. Kärger and J. Haase, *J. Phys. Chem. C*, 2023, **127**, 19833–19840.
52 W. J. Malfait and X. Xue, *Geochim. Cosmochim. Acta*, 2010, **74**, 719–737.
53 A. Kaiser, M. Lobert and R. Telle, *J. Eur. Ceram. Soc.*, 2008, **28**, 2199–2211.
54 M. Andrianainarivelo, R. Corriu, D. Leclercq, P. H. Mutin and A. Vioux, *J. Mater. Chem.*, 1996, **6**, 1665–1671.
55 F. Del Monte, W. Larsen and J. D. Mackenzie, *J. Am. Ceram. Soc.*, 2000, **83**, 1506–1512.
56 R. A. B. Devine, *J. Non-Cryst. Solids*, 1993, **152**, 50–58.
57 C. J. Brinker, R. K. Brow, D. R. Tallant and R. J. Kirkpatrick, *J. Non-Cryst. Solids*, 1990, **120**, 26–33.
58 S. W. Lee and R. A. Condrate, *J. Mater. Sci.*, 1988, **23**, 2951–2959.
59 J. Anderson, C. Fergusson, I. Rodriguezramos and A. Guerreroruiz, *J. Catal.*, 2000, **192**, 344–354.
60 J. B. Miller and E. I. Ko, *J. Catal.*, 1996, **159**, 58–68.
61 E. R. H. van Eck, M. E. Smith and S. C. Kohn, *Solid State Nucl. Magn. Reson.*, 1999, **15**, 181–188.
62 S. K. Lee, *J. Phys. Chem. B*, 2004, **108**, 5889–5900.
63 D. R. Spearing, I. Farnan and J. F. Stebbins, *Phys. Chem. Miner.*, 1992, **19**, 307–321.
64 X. Xue, J. F. Stebbins and M. Kanzaki, *Am. Mineral.*, 1994, **79**, 31–42.
65 Y.-S. Kwon, K. B. Gerasimov and S.-K. Yoon, *J. Alloys Compd.*, 2002, **346**, 276–281.
66 L. Takacs and J. S. McHenry, *J. Mater. Sci.*, 2006, **41**, 5246–5249.
67 H. E. Gottlieb, V. Kotlyar and A. Nudelman, *J. Org. Chem.*, 1997, **62**, 7512–7515.
68 J.-H. Choy, J.-B. Yoon, H. Jung and J.-H. Park, *J. Porous Mater.*, 2004, **11**, 123–129.
69 O. B. Lapina, D. F. Khabibulin and V. V. Terskikh, *Solid State Nucl. Magn. Reson.*, 2011, **39**, 47–57.
70 S. K. Lee and J. F. Stebbins, *Am. Mineral.*, 1999, **84**, 937–945.
71 K. Gobindlal, Z. Zujovic, P. Yadav, J. Sperry and C. C. Weber, *J. Phys. Chem. C*, 2021, **125**, 20877–20886.
72 M. Hasegawa, T. Ogata and M. Sato, *Powder Technol.*, 1995, **85**, 269–274.

